Scripta Materialia 163 (2019) 19–23

Contents lists available at ScienceDirect

Scripta Materialia

journal homepage: www.elsevier.com/locate/scriptamat

Oxygen vacancy ordering and viscoelastic mechanical properties of doped ceria ceramics

Maxim Varenik [a], Sidney Cohen [b], Ellen Wachtel [a], Anatoly I. Frenkel [c], Juan Claudio Nino [d], Igor Lubomirsky [a,*]

[a] Dept. Materials & Interfaces, Weizmann Institute of Science, Rehovot 76100, Israel
[b] Department of Chemical Research Support, Weizmann Institute of Science, Rehovot 76100, Israel
[c] Dept. Materials Science and Chemical Engineering, Stony Brook University, Stony Brook, NY 11794, USA
[d] Department of Materials Science and Engineering, University of Florida, Gainesville, FL, USA

ARTICLE INFO

Article history:
Received 26 September 2018
Received in revised form 15 December 2018
Accepted 16 December 2018
Available online xxxx

Keywords:
Sm-doped ceria
Mechanical properties
Anelasticity
Sound velocity
Nanoindentation

ABSTRACT

Young's, shear and bulk moduli of $Ce_{1-x}Sm_xO_{2-x/2}$ ($x \le 0.55$) were studied using ultrasonic time of flight and nano-indentation techniques. Sound velocity measurements, corrected for sample porosity, demonstrate decrease in the unrelaxed ceramic moduli with increasing Sm-content. Room temperature creep under indenter load-hold, as well as time-dependent material stiffness, reveal a transition from prominent anelasticity in the fluorite phase to prominent elasticity in the double fluorite phase. This supports rearrangement of elastic dipoles under anisotropic stress, which occurs more readily when oxygen vacancies are not ordered on the crystal lattice, as the source of ceria anelastic behavior.

The family of trivalent cation-doped ceria ceramics comprises some of the best and most extensively studied medium temperature (400–800 °C) oxygen ion conductors [1–5], finding application in both solid oxide fuel cells and oxygen sensors. The components in these devices experience both anisotropic and isotropic stress from a variety of sources (thermal, chemical, weight bearing) [6]. However, while the unusually high ionic conductivity of samarium doped ceria (SmDC) has been well characterized [1–5,7], its mechanical properties are still subject to active experimental and theoretical research [5,6,8–24]. This is due to the fact that how, and to what extent, the mechanical properties of ceria ceramics depend on composition, *i.e.* the concentration of point lattice defects and their distribution, is far from being well understood.

A unique feature of the mechanical properties of trivalent rare-earth doped ceria, in comparison to other ceramics, is room temperature anelasticity. In describing the behavior of an anelastic material, the time dependence of the response to stress, particularly anisotropic stress, is an essential parameter. This behavior is attributed to the rearrangement of local, symmetry-lowering distortions in the lattice, which for ceria, are primarily associated with oxygen vacancies [11,12,25–30]. On time scales ≤2 s, rearrangement of point defects is too slow to affect mechanical properties and consequently, unrelaxed moduli are observed. In fact, relaxation times may range from a few seconds to a few weeks, depending on the morphology, thermal history and chemistry of the material. In the fully relaxed state, the biaxial elastic modulus of doped ceria thin films has been observed to be as much as a factor of ten lower than that observed for the unrelaxed modulus [5,11,12,25,26].

The unrelaxed moduli of doped ceria have been measured by a number of researchers using a variety of techniques [5,10,11,13,31–34]. Those moduli which are derived from sound velocity measurements in dense ceramics, such as the impulse excitation technique [8] and ultrasonic pulse-echo time of flight (USTOF) [5,10], demonstrate that moduli decrease with dopant concentration. As an example, in Gd-doped ceria, Young's and shear moduli decrease 0.48 ± 0.03% per mol % Gd for $x < 0.3$, which is the upper dopant limit of the stability of the fluorite ($Fm\bar{3}m$) phase. In the double fluorite ($Ia\bar{3}$) phase $x \ge 0.3$, the normalized Young's and shear moduli of Gd-doped ceria ceramics are larger than the value extrapolated from the linear dependence observed in the fluorite phase. However, all the data for the bulk modulus, including that for $x = 0.3$, follow a linear decrease.

On the other hand, nanoindentation-based measurements of the Young's modulus are performed on a time scale of a few tens of seconds [4,9,11,12,34,35]. This is slow enough for ceria anelasticity to become evident, and therefore, the outcome of such measurements depends on the loading/unloading rates. Faster loading has been observed to produce more consistent results than slower loading [11,12]. Nevertheless, the reproducibility of such measurements usually does not exceed ±5%, thereby masking the relatively weak

* Corresponding author.
E-mail address: Igor.Lubomirsky@weizmann.ac.il (I. Lubomirsky).

https://doi.org/10.1016/j.scriptamat.2018.12.024
1359-6462/

dependence on dopant concentration. Aliovalent doped ceria also shows noticeable room temperature creep [11,12], the magnitude of which depends on the type and concentration of the dopant.

In the present work, mechanical properties of aliovalent-doped ceria ceramics with 5–55 mol% Sm were investigated using USTOF and nanoindentation techniques. At high Sm concentrations, the term 'doping' may not be appropriate to describe the solid solution of $SmO_{1.5}/CeO_2$. However, as this is the commonly used terminology in the ceramic and solid state literature, it will be used for both high and low concentration samples described in this report. The ionic radius of Sm^{3+} is similar to that of Gd^{3+} (122 pm and 119 pm, respectively). However, the transition from fluorite to double fluorite symmetry is only detected by X-ray diffraction for concentrations above 35 mol% Sm (Fig. S1), while for Gd doped ceria, this transition occurs above 20 mol% dopant. With 40 mol% Sm^{3+} [7,14], the XRD pattern may be indexed as double fluorite, in which both cations and anions occupy two inequivalent lattice sites and oxygen vacancies are no longer randomly distributed. With the extended concentration range x = 0.05–0.55, there are sufficient data to observe the mechanical behavior of the ceramic pellets in both phases.

Ceramic pellets of $Ce_{1-x}Sm_xO_{2-x/2}$ ($0.05 \le x \le 0.55$, at 0.05 increments) were synthesized from 99.99% purity powders of Sm_2O_3 and CeO_2 *via* conventional solid-state reactions as described previously [7]. The powders were ball-milled, dried and calcined at 1450 °C for 10 h. Up to 2% w/w binder (PVA dissolved in deionized water) was added to the powders and disk-shaped pellets (height > 1 mm, diameter ~8 mm) were formed in dies by uniaxial pressing. The pellets were then subjected to isostatic pressing at 250 MPa for 3 min and sintered at 1600 °C for 10 h ($0.05 \le x \le 0.25$) or 1690 °C for 5 h ($0.30 \le x \le 0.55$), respectively. All samples were reoxygenated prior to mechanical measurement by heating at 500 °C for 5 h in a pure oxygen environment. The average grain sizes, as determined from SEM images using the linear intercept method with correction factor 1.56 [36,37], range from 10 to 25 μm without obvious dependence on Sm concentration (Fig. S2). X-ray diffraction (XRD) patterns of the pellets were acquired with a Rigaku Ultima III θ–θ diffractometer in Bragg–Brentano configuration. The unit cell parameter (a) was calculated using Jade 10 software (MDI, CA). Porosity (p) is defined as $(1-\rho_m/\rho_{th})$ where the XRD-determined unit cell volume and known content was used to calculate the theoretical lattice density, ρ_{th}. The experimental density, ρ_m, of the sintered pellets was measured with the Archimedes technique using deionized water (18 MΩ · cm) as working liquid. The presence of very small amounts of residual PVA ash in the ceramic pellets did not affect mechanical behavior.

Shear (transverse, V_S) and longitudinal, (V_L) sound velocities were determined with accuracy better than 0.25% from pellet height, measured with uncertainty ≤0.15% and the ultrasound time of flight (TOF), τ, as described in [38] and in Supplementary (Eqs. (S1)–(S2)). The TOF was measured using an appropriate transducer coupled directly to the pellets with high viscosity commercial honey without external force. Correction for porosity <6 vol% was performed as described previously [10]. The two models, static and dynamic, are detailed in the Supplementary file (Eqs. (S3)–(S4)).

Nanoindentation measurements were carried out at room temperature using an Agilent-XP instrument with diamond Berkovich-tip indenter. To minimize effects of surface inhomogeneity, all measurements were performed with indentation depth ≥ 700 nm and at ≥10 locations on each sample. To ensure that the upper indentation limit is much smaller than the average grain size, indentation depth did not exceed 1100 nm (Supplementary, Fig. S2). Measurements were performed using a protocol described previously [11,12] with a trapezoidal load–hold–unload cycle. The "fast" loading rate was 15 mN/s to maximum load 150 mN and the "slow" loading, as well as unloading, rates were 0.15 mN/s to 150 mN load. Load-hold time was either 8 s (*fast*) or 30 s (*slow*) at maximum load before retracting the indenter. The material stiffness (S) was determined from the initial slope of the unloading phase of the cycle using Oliver - Pharr analysis for elastic solids [39,40]. Young's modulus is linearly proportional to S. In contrast to Gd, Pr^{3+} and Lu-doped ceria [11,12], for which 15mN/s unloading rate produced useful data, for Sm-doped ceria, *fast* unloading rates >5 mN/s produced a negative slope upon indenter retraction, rendering the results unsuitable for modulus calculation. Loading and unloading curves selected for calculations were smooth without "pop-ins" or instabilities. Thermal drift rates measured in separate experiments at 90% unloading were <0.1 nm/s and did not significantly influence the results.

XRD patterns of $Ce_{1-x}Sm_xO_{2-x/2}$ pellets (Fig. S1) demonstrate that ceramics with $x < 0.35$ are in the fluorite phase while for $x > 0.4$, appearance of additional peaks clearly indicates transformation into the double fluorite phase. The intensity of these peaks increases for $x > 0.4$. The lattice parameters measured are close to previously reported values [3,7,14,27]. Porosity of the pellet samples, calculated as described above (Fig. 1, inset), was within the acceptable limit (<6 vol%) except for Sm concentrations between $x = 0.3$–0.45. Interestingly, concentrations for which high porosity is observed coincide with the transition region between the fluorite and the double fluorite phases, which has been termed the 'hybrid' region [14] based on Rietveld analysis of Sm-doped ceria powders. For sintered pellets, coarsening appears to be much more rapid than densification in the 'hybrid' region, suggesting high mobility of grain boundaries [41].

The uncorrected elastic moduli deduced from the longitudinal (V_L) and shear (V_S) sound velocities (Fig. 1), and Eqs. (S1) and (S2) do not show consistent dependence on Sm concentration. However, after correcting for porosity (Eqs. (S3)–(S4)), a monotonic decrease is clearly visible. In the intermediate concentration range $0.3 \le x \le 0.45$, high porosity prevents accurate determination of the elastic moduli (Fig. 2, shaded regions) and Poisson's ratio (Fig. S4, shaded region). In the fluorite phase ($x \le 0.25$) all moduli decrease with Sm content (Fig. 2). This is not unexpected, as increased Sm concentration leads to lattice expansion and reduction in the number of chemical bonds due to vacancy formation [27,31,42]. The rate of decrease of the Young's, shear and bulk moduli, normalized to those of the undoped pellet, is ~ 0.5% per mol% Sm (Fig. 2d, Table 1), similar to that observed for Gd-doped ceria in the fluorite phase [10]. In the double fluorite phase, x > 0.45, unrelaxed moduli decrease with increase in Sm content at a rate of 0.27% per mol%. This result likely reflects the significantly weaker increase in lattice constant with increased Sm concentration in the double fluorite phase (Fig. S1c). USTOF data for the unrelaxed elastic moduli of Gd^{3+}doped ceria ceramics are not yet available.

Fig. 3a shows indenter displacement and applied load observed for a 10 mol% Sm-doped ceramic pellet as a function of time with 15 mN/s loading rate and 5 mN/s unloading rate. Young's moduli, derived according to standard Oliver-Pharr protocol from the initial slope of

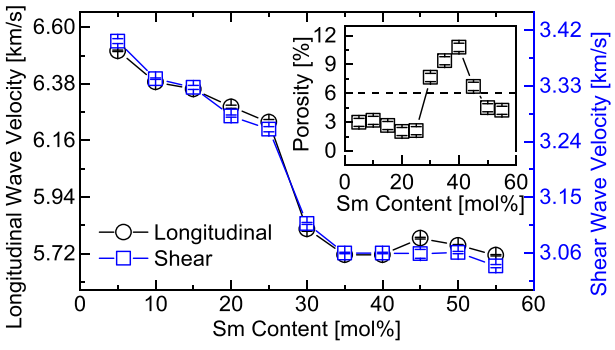

Fig. 1. Longitudinal (left, black) and shear (right, blue) sound wave velocity in Sm doped ceria as derived from ultrasound pulse echo time of flight (USTOF) measurements. Inset: pellet porosity as a function of Sm content. Theoretical density was calculated using the XRD measured lattice parameter (Fig. S1) and the known contents of the unit cell; pellet density was measured using the Archimedes method as described in the text. (For interpretation of the references to colour in this figure legend, the reader is referred to the web version of this article.)

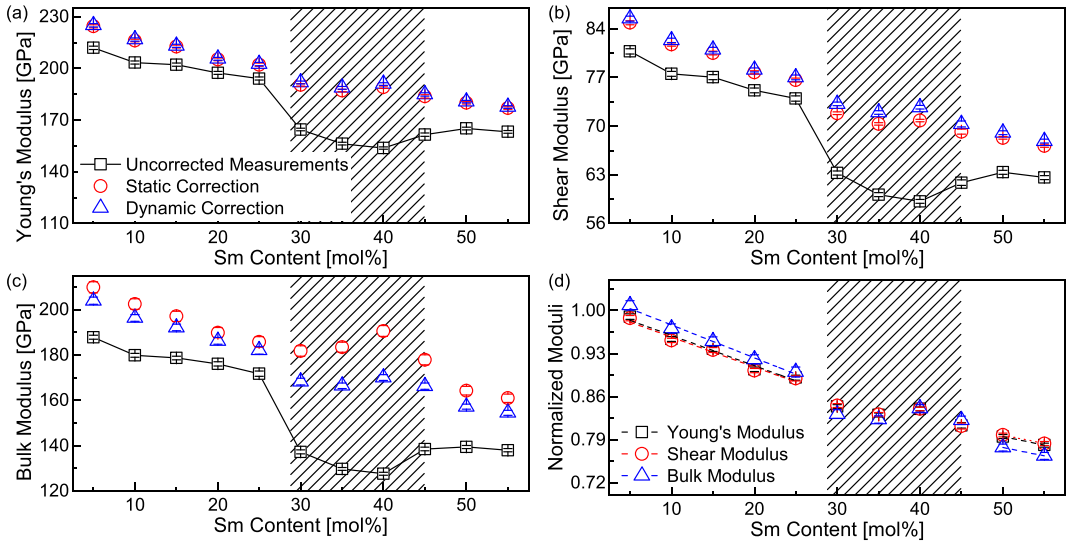

Fig. 2. Uncorrected and porosity-corrected (a) Young's, (b) shear and (c) bulk moduli as calculated from USTOF measurements (Fig. S1). Black squares – uncorrected values; red circles – static correction according to [43]; and blue triangles - dynamic correction according to Ledbetter, [44,45] (d) Normalized (to dopant-free values) Young's, shear and bulk moduli, following porosity correction [44,45]. The linear slopes, in % per mol% Sm, for the normalized Young's, shear and bulk moduli are presented in Table 1. Shaded areas indicate samples with porosity >6%, for which correction cannot be reliably made. (For interpretation of the references to colour in this figure legend, the reader is referred to the web version of this article.)

unloading curves (Fig. 3b), show large differences between "slow" (0.15mN/s) and "fast" (5mN/s) unloading rates (Fig. 4a). This obvious dependence on time is characteristic of viscoelastic (*e.g.*, anelastic) solids; the Young's modulus and surface hardness (H) determined by NI can be artificially high. However, by applying modified analytical procedures [46,47], it is possible to extract the elastic contribution to the material stiffness S and contact depth h_c and thereby, a more accurate relaxed Young's modulus and surface hardness (Fig. S5) may be obtained. Most importantly, with this correction, the "fast" nanoindentation measurements are clearly able to show that the anelastic properties of Sm doped ceria become significantly weaker as dopant concentration increases (Fig. 4b). As the elastic contribution increases, the "fast" and "slow" NI measurements of the Young's modulus begin to overlap (Fig. 4a), and both approach the unrelaxed modulus measured with USTOF (Fig. 4a). However, NI error bars are still too large to enable detection of the dependence of the Young's modulus on Sm concentration with the same level of confidence as the USTOF technique. NI data for Gd-doped ceria [11] are only available in the fluorite phase.

With 'fast' loading, room temperature creep (*i.e.*, continued displacement at constant load, a marker for viscoelastic behavior) is clearly visible on the load-hold segment of the nanoindentation curves (*viz.*, Fig. 3a,b). As in the case of Gd-doped ceria [11,12] and (Nb,Y)-stabilized Bi_2O_3 [10], displacement, η, follows time dependence typical of primary creep [48]:

$$\eta - \eta_0 = A \cdot \sqrt[3]{t - t_0} \quad (1)$$

where η_0 is displacement at the beginning of the hold stage at time t_0 (inset) and A is the creep constant [15]. The creep constant remains unchanged, to within experimental uncertainty, for x < 0.10; at higher Sm concentrations, it decreases until a plateau is reached for x > 0.25 (Fig. 4c). Therefore, both the creep constant and the Young's modulus, as measured by NI, provide a self-consistent picture of a measurably more elastic mechanical behavior in the more heavily Sm-doped ceria ceramics (Fig. 4b).

Table 1
Rates of decrease of Young's, shear and bulk moduli in Sm doped ceria.

	Normalized slope x < 0.3	Normalized slope x > 0.5
Young's modulus	−0.53 ± 0.03	−0.27 ± 0.01
Shear modulus	−0.49 ± 0.05	−0.28 ± 0.01
Bulk modulus	−0.49 ± 0.04	−0.27 ± 0.02

Slopes are in units of % per mol% dopant.

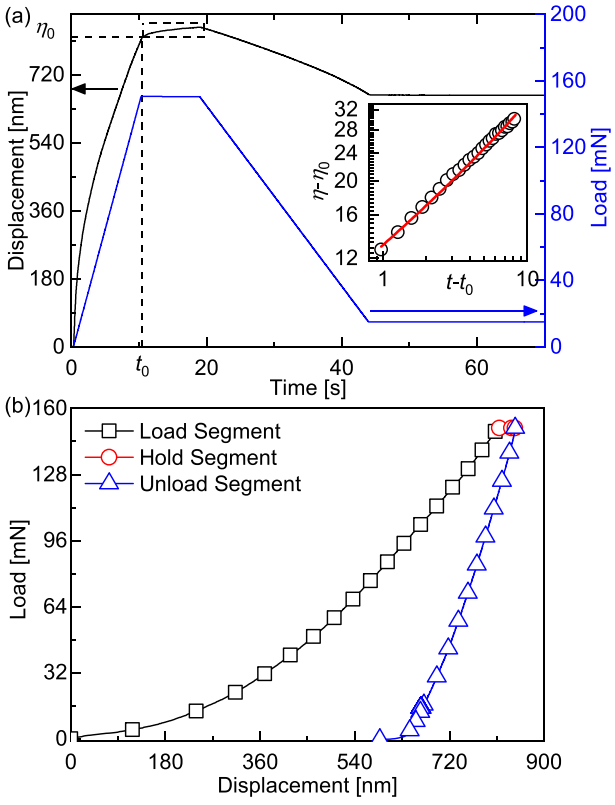

Fig. 3. (a) Indenter displacement (left, black) and load on sample (right, blue) during a *fast* nanoindentation measurement on a 10 mol% Sm doped ceria pellet at room temperature; the primary creep observed in the hold phase (dashed rectangle in (a)), and a graph inset of the matching power law fit of 1/3 (red line, fit to Eq. (1)). Creep is also observed in load-displacement curves (b) as an increase in displacement at maximum load. (For interpretation of the references to colour in this figure legend, the reader is referred to the web version of this article.)

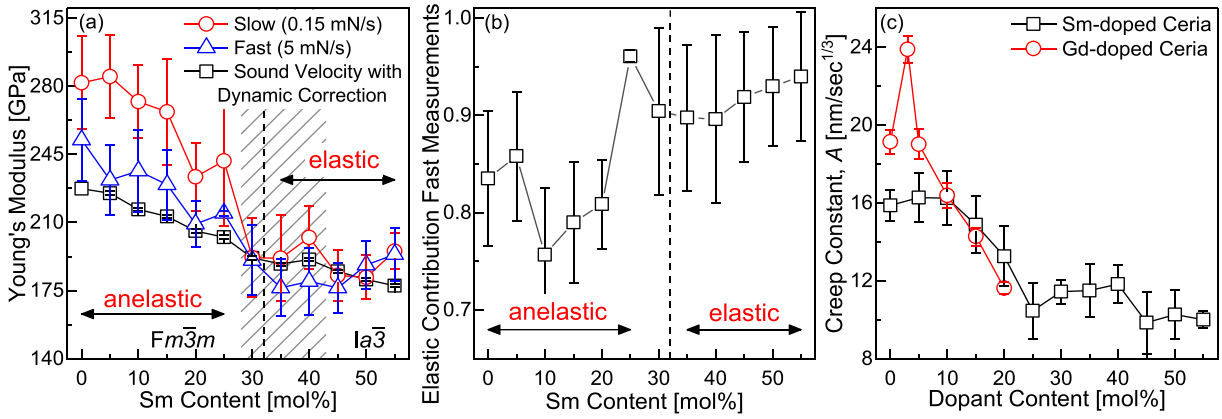

Fig. 4. (a) Young's modulus as a function of Sm content calculated according to standard Oliver-Pharr protocol from the *fast* (5 mN/s; blue triangle) and *slow* (0.15 mN/s; red circle) nanoindentation load-release curves. Moduli calculated from porosity-corrected sound velocity measurements are given for comparison (□). The shaded region denotes samples with porosity that is too high to be reliably corrected. The dashed vertical line indicates the first XRD observation of the fluorite → double fluorite transition (Fig. S1). (b) The elastic component of the NI-determined Young's modulus for 5 mN/s unloading rate, calculated according to the treatment for visco-elastic materials presented in [46,47]. Clearly, the anelasticity of the ceramic samples decreases as the concentration of Sm^{3+} and oxygen vacancies increases. (c) Room temperature creep constant (A) calculated from the 'fast' NI measurements for Sm- or Gd-doped [11] ceria ceramics as a function of dopant-content. The loading rates for both are 15 mN/s and load-hold, 8 s. Error bars are standard deviation of ≥10 measurements at different locations on the surface of the same pellet. (For interpretation of the references to colour in this figure legend, the reader is referred to the web version of this article.)

The structural interpretation of this behavior is similar to that given earlier [11,12]: *i.e.*, room temperature creep results from stress-induced rearrangement of local strain fields associated with oxygen vacancies V_O [19,27,49,50]. In Gd-doped ceria, x < 0.2, in the absence of external stress or electric field, modeling has shown that the randomly distributed dipolar strain fields do not have a preferred direction [49]. The distorted 8-atom complexes, containing $7O\text{-}Ce_{Ce}\text{–}Vo$, are able to rearrange on a time scale of a few tens of seconds in response to anisotropic stress induced by, *e.g.*, nanoindentation [11,12] or an electric field [49]. If the time scale of the applied load is shorter than the time necessary for the [20,25,26] complexes to rearrange, then during the "load-hold" stage of the cycle, continued rearrangement produces room temperature creep. If loading is slow enough for the complexes to rearrange, then room temperature creep is diminished. In the double fluorite phase, oxygen vacancy ordering apparently stiffens the lattice, thereby reducing the mobility of the local dipolar strain fields, and consequently producing more prominently elastic material properties: little or no rearrangement is possible.

Unrelaxed Young's, shear and bulk moduli of $Ce_{1-x}Sm_xO_{2-x/2}$, $0.05 \le x \le 0.55$, derived from ultrasound pulse echo measurement of longitudinal and transverse sound velocity, decrease with increase in samarium content. The lower moduli are due in part to lattice expansion as well as to the decrease in the number of chemical bonds resulting from oxygen vacancy formation. The importance of loading/unloading rates during nanoindentation points to the influence of viscoelastic perturbation to the determination of Young's modulus using the Oliver- Pharr protocol. The measurements of relaxed\unrelaxed moduli reported here may indeed provide more realistic constraints for atomistic modeling of the anelasticity and mechanical properties of ceria, the understanding of which remains far from complete [51,52]. Correcting Young's modulus and hardness values according to literature treatments of viscoelastic materials, shows that anelasticity plays a larger role in the fluorite phase where the oxygen vacancies are more randomly distributed on the lattice than in the double fluorite phase where ordering begins to take place: *i.e.* oxygen vacancy ordering stiffens the lattice.

IL and AIF acknowledge the NSF-BSF program grant 2015679. AIF acknowledges support by NSF Grant number DMR-1701747. This work was supported in part by the Israeli Ministry of Science and Technology grant 3-12944. This research is made possible in part by the historic generosity of the Harold Perlman Family.

Appendix A. Supplementary data

Supplementary data for this article can be found online at https://doi.org/10.1016/j.scriptamat.2018.12.024.

References

[1] J. Molenda, K. Swierczek, W. Zajac, J. Power Sources 173 (2) (2007) 657–670.
[2] N. Mahato, A. Banerjee, A. Gupta, S. Omar, K. Balani, Prog. Mater. Sci. 72 (2015) 141–337.
[3] P. Ramos-Alvarez, M.E. Villafuerte-Castrejon, G. Gonzalez, M. Cassir, C. Flores-Morales, J.A. Chavez-Carvayar, J. Mater. Sci. 52 (1) (2017) 519–532.
[4] J.G. Swallow, J.J. Kim, M. Kabir, J.F. Smith, H.L. Tuller, S.R. Bishop, K.J. Van Vliet, Acta Mater. 105 (2016) 16–24.
[5] E. Wachtel, I. Lubomirsky, Scr. Mater. 65 (2) (2011) 112–117.
[6] R. Bove, S. Ubertini, Modeling Solid Oxide Fuel Cells: Methods, Procedures and Techniques, Springer, Berlin, 2008.
[7] L.P. Li, J.C. Nino, J. Eur. Ceram. Soc. 32 (13) (2012) 3543–3550.
[8] A. Atkinson, T.M.G.M. Ramos, Solid State Ionics 129 (1–4) (2000) 259–269.
[9] Y.L. Wang, K. Duncan, E.D. Wachsman, F. Ebrahimi, Solid State Ionics 178 (1–2) (2007) 53–58.
[10] N. Yavo, D. Noiman, E. Wachtel, S. Kim, Y. Feldman, I. Lubomirsky, O. Yeheskel, Scr. Mater. 123 (2016) 86–89.
[11] R. Korobko, C.T. Chen, S. Kim, S.R. Cohen, E. Wachtel, N. Yavo, I. Lubomirsky, Scr. Mater. 66 (3–4) (2012) 155–158.
[12] R. Korobko, S.K. Kim, S. Kim, S.R. Cohen, E. Wachtel, I. Lubomirsky, Adv. Funct. Mater. 23 (48) (2013) 6076–6081.
[13] K. Amezawa, T. Kushi, K. Sato, A. Unemoto, S. Hashimoto, T. Kawada, Solid State Ionics 198 (1) (2011) 32–38.
[14] C. Artini, M. Pani, M.M. Carnasciali, J.R. Plaisier, G.A. Costa, Inorg. Chem. 55 (20) (2016) 10567–10579.
[15] I.C. Choi, B.G. Yoo, Y.J. Kim, J.I. Jang, J. Mater. Res. 27 (1) (2012) 2–10.
[16] P.M. Claesson, I. Dobryden, G. Li, Y.J. He, H. Huang, P.A. Thoren, D.B. Haviland, Phys. Chem. Chem. Phys. 19 (35) (2017) 23642–23657.
[17] X.F. Fan, E.D. Case, Q. Yang, J.D. Nicholas, Ceram. Int. 39 (6) (2013) 6877–6886.
[18] A.C. Fischer-Cripps, Nanoindentation, 3rd ed. Springer, New York, 2011.
[19] A. Kossoy, A.I. Frenkel, Y. Feldman, E. Wachtel, A. Milner, I. Lubomirsky, Solid State Ionics 181 (33–34) (2010) 1473–1477.
[20] T. Das, J.D. Nicholas, B.W. Sheldon, Y. Qi, Phys. Chem. Chem. Phys. 20 (22) (2018) 15293–15299.
[21] S. Schweiger, R. Pfenninger, W.J. Bowman, U. Aschauer, J.L.M. Rupp, Adv. Mater. 29 (15) (2017).
[22] Y.Z. Shi, K.H. Stone, Z.X. Guan, M. Monti, C.T. Cao, F. El Gabaly, W.C. Chueh, M.F. Toney, Phys. Rev. B 94 (20) (2016).
[23] Y.Z. Shi, S.C. Lee, M. Monti, C. Wang, Z.L.A. Feng, W.D. Nix, M.F. Toney, R. Sinclair, W.C. Chueh, ACS Nano 10 (11) (2016) 9938–9947.
[24] K.M. Kant, V. Esposito, N. Pryds, Appl. Phys. Lett. 100 (3) (2012).
[25] M. Greenberg, E. Wachtel, I. Lubomirsky, J. Fleig, J. Maier, Adv. Funct. Mater. 16 (1) (2006) 48–52.
[26] A. Kossoy, Y. Feldman, E. Wachtel, I. Lubomirsky, J. Maier, Adv. Funct. Mater. 17 (14) (2007) 2393–2398.
[27] A. Kossoy, Q. Wang, R. Korobko, V. Grover, Y. Feldman, E. Wachtel, A.K. Tyagi, A.I. Frenkel, I. Lubomirsky, Phys. Rev. B 87 (5) (2013).
[28] T. Zacherle, A. Schriever, R.A. De Souza, M. Martin, Phys. Rev. B 87 (13) (2013).

[29] M. Martin, T. Zacherle, A. Schriever, R.A. De Souza, S. Grieshammer, Solid Oxide Fuel Cells 13 (Sofc-Xiii) 57 (1) (2013) 2405–2410.
[30] R.A. De Souza, M. Martin, Monatsh. Chem. 140 (9) (2009) 1011–1015.
[31] M.J.D. Rushton, A. Chroneos, J. Mater. Sci. Mater. Electron. 24 (11) (2013) 4590–4592.
[32] K. Sato, H. Yugami, T. Hashida, J. Mater. Sci. 39 (18) (2004) 5765–5770.
[33] T. Ishida, F. Iguchi, K. Sato, T. Hashida, H. Yugami, Solid State Ionics 176 (31–34) (2005) 2417–2421.
[34] M. Morales, J.J. Roa, X.G. Capdevila, M. Segarra, S. Pinol, Acta Mater. 58 (7) (2010) 2504–2509.
[35] M. Lipinska-Chwalek, F. Schulze-Kuppers, J. Malzbender, J. Eur. Ceram. Soc. 35 (5) (2015) 1539–1547.
[36] M.I. Mendelson, J. Am. Ceram. Soc. 52 (8) (1969) 443.
[37] C.S. Smith, L. Guttman, JOM 5 (1) (1953) 81–87.
[38] O. Yeheskel, O. Tevet, J. Am. Ceram. Soc. 82 (1) (1999) 136–144.
[39] W.C. Oliver, G.M. Pharr, J. Mater. Res. 7 (6) (1992) 1564–1583.
[40] W.C. Oliver, G.M. Pharr, J. Mater. Res. 19 (1) (2004) 3–20.
[41] R.M. German, Crit. Rev. Solid State 35 (4) (2010) 263–305.
[42] J. Pelleg, Mechanical properties of ceramics, Springer Science & Business (2014).
[43] R. Pal, J. Compos. Mater. 39 (13) (2005) 1147–1158.
[44] H.M. Ledbetter, S.K. Datta, J. Acoust. Soc. Am. 79 (2) (1986) 239–248.
[45] H.M. Ledbetter, M.W. Austin, S.A. Kim, M. Lei, J. Mater. Res. 2 (6) (1987) 786–789.
[46] G. Feng, A.H.W. Ngan, J. Mater. Res. 17 (3) (2002) 660–668.
[47] A.H.W. Ngan, B. Tang, J. Mater. Res. 17 (10) (2002) 2604–2610.
[48] H. Li, A.H.W. Ngan, J. Mater. Res. 19 (2) (2004) 513–522.
[49] Y.Y. Li, O. Kraynis, J. Kas, T.C. Weng, D. Sokaras, R. Zacharowicz, I. Lubomirsky, A.I. Frenkel, AIP Adv. 6 (5) (2016).
[50] R. Korobko, A. Lerner, Y.Y. Li, E. Wachtel, A.I. Frenkel, I. Lubomirsky, Appl. Phys. Lett. 106 (4) (2015).
[51] P.A. Zguns, A.V. Ruban, N.V. Skorodumova, Scr. Mater. 158 (2019) 126–130.
[52] E. Wachtel, A.I. Frenkel, I. Lubomirsky, Adv. Mater. 30 (41) (2018).